Moment tensor potential and its application in the Ti-Al-V multicomponent system

Mashroor S. Nitol,[1,*] Avanish Mishra,[2] Shuozhi Xu,[3] and Saryu J. Fensin[1]

[1]*Center for Integrated Nanotechnologies, Los Alamos National Laboratory, Los Alamos, New Mexico 87544, USA*

[2]*Theoretical Division (T-1), Los Alamos National Laboratory, Los Alamos, New Mexico 87545, USA*

[3]*School of Aerospace and Mechanical Engineering, University of Oklahoma, Norman, Oklahoma 73019-1052, USA*

(Received 21 February 2025; revised 12 May 2025; accepted 27 May 2025; published 3 June 2025)

Titanium (Ti) alloys such as Ti-6Al-4V are recognized as critical materials for aerospace and biomedical applications due to their exceptional strength-to-weight ratio and high-temperature performance. Traditional interatomic potentials are known to struggle in capturing their complex phase behavior, limiting atomistic modeling capabilities. In this work, a machine learning (ML)-based moment tensor potential (MTP) is developed using first-principles data from diverse configurations that span the unary, binary, and ternary systems of Ti, Al, and V. The optimized MTP is shown to achieve accuracy of density functional theory (DFT) level for lattice parameters (errors $<1.2\%$), elastic constants (errors $<10\%$ for most components), and stack fault energies, while having computational efficiency comparable to non-ML potentials. Phase stability across composition-temperature space is predicted through hybrid Monte Carlo (MC)/molecular dynamics simulations, including α/β transitions in pure Ti (1083 K vs. experimental 1155 K), α-to-$D0_{19}$ transitions in Ti-Al (8.5–25 at.% Al), and $\beta+\omega$ coexistence in Ti-V alloys. In particular, the evolution of the β precipitate in Ti-6Al-4V is captured by MTP without explicit training on ternary DFT-MC data. This work establishes the MTP framework as a powerful tool for modeling complex phase transformations in multicomponent Ti alloys, enabling atomistic insights into microstructural evolution and alloy design.

DOI: 10.1103/PhysRevMaterials.9.063601

I. INTRODUCTION

Titanium (Ti) alloys, including the Ti-Al-V system, have become critical in a wide range of industry sectors, including aerospace, petrochemical, marine, and medical [1]. These alloys possess an excellent strength-to-weight ratio, resistance to high temperatures, exceptional corrosion resistance, and biocompatibility, leading to their applications from jet engine components to medical implants [2]. Among structural materials, Ti alloys are unique, with a melting point of ~1973 K and a density of approximately 4.5 g/cc, while the tensile strength of some grades exceeds 1500 MPa at room temperature [3].

The phase behavior of the Ti-Al-V alloy system is highly complex as a result of the underlying thermodynamic and kinetic phenomena. These include diffusion-controlled phase transformations, the competition between nucleation and growth of different phases, and the influence of elastic strain energy at phase interfaces. A key feature of these alloys is their allotropic transformation, where Ti transitions from a hexagonal close-packed phase (HCP) α to a body-centered cubic (BCC) β phase at approximately 1163 K. This transformation is governed by atomic rearrangement and diffusion kinetics, which are further influenced by alloying elements such as Al and V. The precipitation and coarsening mechanisms of the α and β phases, driven by differences in Gibbs free energy and atomic mobility, enable precise tailoring of mechanical properties.

For example, dual-phase $\alpha+\beta$ alloys are widely used in aerospace applications, as Ti-6Al-4V offers a balance of high-temperature strength, corrosion resistance, and machinability [4,5]. The alloy constituent elements control phase stability; additions of Al increase the α-to-β transformation temperature, thus acting as an α stabilizer, while V lowers this temperature, serving as a β stabilizer [6].

This further extends the utility of the Ti-Al-V alloy system, as diffusion kinetics and phase transformation pathways can be controlled through appropriate heat treatment [7]. Controlled cooling from the β phase region may lead to the formation of metastable martensitic structures, where rapid quenching suppresses diffusional phase transformations and promotes shear-driven phase transformations. In contrast, a slower cooling rate allows sufficient atomic diffusion, leading to the formation of equiaxed α grains, which enhance ductility and fatigue resistance. Additionally, stress-induced transformations and phase stability under mechanical loads play a crucial role in determining the material's performance.

In principle, such a structure is desirable; however, precise regulation of processing conditions—such as heat treatment parameters, alloy composition, and thermomechanical processing—is necessary to prevent the formation of brittle phases such as the ω phase, which results from a diffusionless transformation involving local atomic rearrangements within the BCC lattice [8,9]. The mechanical properties of these materials, including their resistance to fatigue and creep, are influenced by microstructural characteristics such as the colony structures of the α phase and the distribution of the transformed β phases [10,11].

*Contact author: mash@lanl.gov

 ©2025 American Physical Society

To understand these physical phenomena on an atomistic scale, such as phase nucleation, diffusion kinetics, and transformation pathways, molecular dynamics (MD) simulations are used as an integral part of computational materials research [12]. By tracking atomic trajectories over time, these simulations provide unique insights into mechanical behavior, phase transitions, the formation of defects, and structural properties of materials under different conditions, such as high-rate deformation, radiation, extreme temperature, etc. For material systems like Ti-Al-V, where the microstructural properties are intricately connected to the performance, such simulations can reveal mechanisms for phenomena observed in experiments. A representation of interatomic interaction is required to perform an MD simulation. The choice of interatomic potential, which is a mathematical model governing interatomic interactions, strongly impacts the quality of MD simulations. Empirical potentials, such as the embedded atom method (EAM) [13] and modified embedded atom method (MEAM) [14,15], are widely used in MD studies but often struggle to capture subtle phase behavior in complex alloys. For example, in Ti-V systems, phase evolution is highly sensitive to V content, making it difficult to model with conventional potentials. The lack of accurate models for complex phase transitions limits the predictive capability of atomistic simulations for alloy design.

Machine learning interatomic potentials (MLIPs) have emerged as an accurate solution to overcome these challenges [16–23]. By using first-principle theoretical datasets, MLIPs can accurately describe the nonlinear and multiscale interactions characteristic of complex alloys. Compared with traditional empirical models, MLIPs allow for the modeling of interatomic interactions with unprecedented accuracy. The quality and diversity of the training datasets are the key factors that determine the performance of MLIPs. A poor or unrepresentative database will result in poor generalization, and hence, MLIPs would become ineffective in predicting occurrences outside the training range. Therefore, in order to unleash the full potential of MLIPs for predictive materials design, it is important to construct exhaustive datasets containing diversified configurations, phases, and compositions.

The moment tensor potential (MTP) exhibits a notable computational advantage compared to other machine learning interatomic potentials (MLIPs) [19], especially when contrasted with deep-learning-based models like the rapid artificial neural network (RANN) [24] and deep potential (DeePMD) [25]. Recent studies indicate that MTP potentials offer significant benefits for modeling alloys, primarily due to their ability to require less training data while delivering enhanced accuracy and improved computational speed. MTP has been shown to exceed other methods in speed while also achieving accuracy comparable to leading MLIPs across various material systems. It has been acknowledged for achieving an effective equilibrium between precision and computational efficiency [26–28]. A binary Ti–Al MTP was recently developed by Qi *et al.* [29], with training focused mainly on intermetallic phases such as $L1_0$-TiAl and $D0_{19}$-Ti_3Al. Challenges were encountered in the process of capturing phase transitions and solute effects within solid solutions [24].

In the current study, the MTP framework [30] has been used to tackle the shortcomings of the previously established Ti–Al potential [29]. A comprehensive and varied dataset is included, comprising ground-state structures, *ab initio* molecular dynamics snapshots, surface configurations, solid solutions, and strained bulk structures for unary, binary, and ternary systems. This approach leads to the development of a Ti–Al–V potential that provides profound insights into intricate ternary behaviors with remarkable precision. The current potential demonstrates remarkable reliability for the Ti-Al-V system, including stable α, β, and metastable $\alpha + \beta$ phases across varied V concentrations. This MTP is the first interatomic potential to thoroughly represent the Ti-Al-V system while accurately replicating essential features of commercial alloys within the Ti-(1-30) at.% Al and %V composition spectrum. Moreover, it precisely forecasts lattice and elastic characteristics, their temperature dependence, surface energies, and γ-lines in both unary systems and intermetallic phases such as $L1_0$-TiAl and $D0_{19}$-Ti_3Al. It also encompasses solute influences in the stacking defects of Ti, representing a notable progression in the development of interatomic potentials for intricate alloy systems.

II. COMPUTATIONAL METHODS

A. Training database and DFT calculations

A dataset with large variation is required to model the complex atomic environment of Ti-Al-V alloys. The Vienna *Ab initio* Simulation Package (VASP) [31], version 6.3.2, using the Perdew-Burke-Ernzerhof functional within the generalized gradient approximation framework [32] for exchange-correlation, was employed to generate the training dataset. A Monkhorst-Pack grid ensured a minimum k-point spacing of $2\pi \times 0.01\,\text{Å}^{-1}$. The electronic wave functions were extended with a kinetic energy cutoff of 520 eV, and Gaussian smearing with a width of 0.2 eV smoothed the Brillouin zone integration. The electronic relaxation converged to an energy threshold of 10^{-6} eV, while ionic relaxation proceeded until the force on each atom was below 0.01 eV/Å.

Following our previous work [33,34], the database includes primitive cell lattice distortions up to 15% from equilibrium for BCC, FCC, HCP, and additional structures (e.g., $a15$, β-Sn, SC, DC) for Al, Ti, and V. Additionally, the database provides shear-distorted unit cells for ordered intermetallic compounds, including examples like γ-TiAl and $D0_{19}$-Ti_3Al. Supercells are constructed with different factors, including random atomic displacements up to 0.5 Å and box size fluctuations of ±5% to simulate thermal perturbations and expansion effects. These configurations include pure elements, Ti-rich Al and V alloys (α, β, ω phases), Al-rich Ti and V alloys (FCC phase), and V-rich Al and Ti alloys (BCC phase), with up to 50% solute content. With these perturbations, temperature effects were modeled from 100 to 2500 K. Similar perturbed structures of Ti-Al intermetallics are included as well.

B. Moment tensor potential

MTP has been applied to a wide variety of materials, including elemental metals and alloys [26,28,35–37]. At its core, MTP describes the local atomic environment using

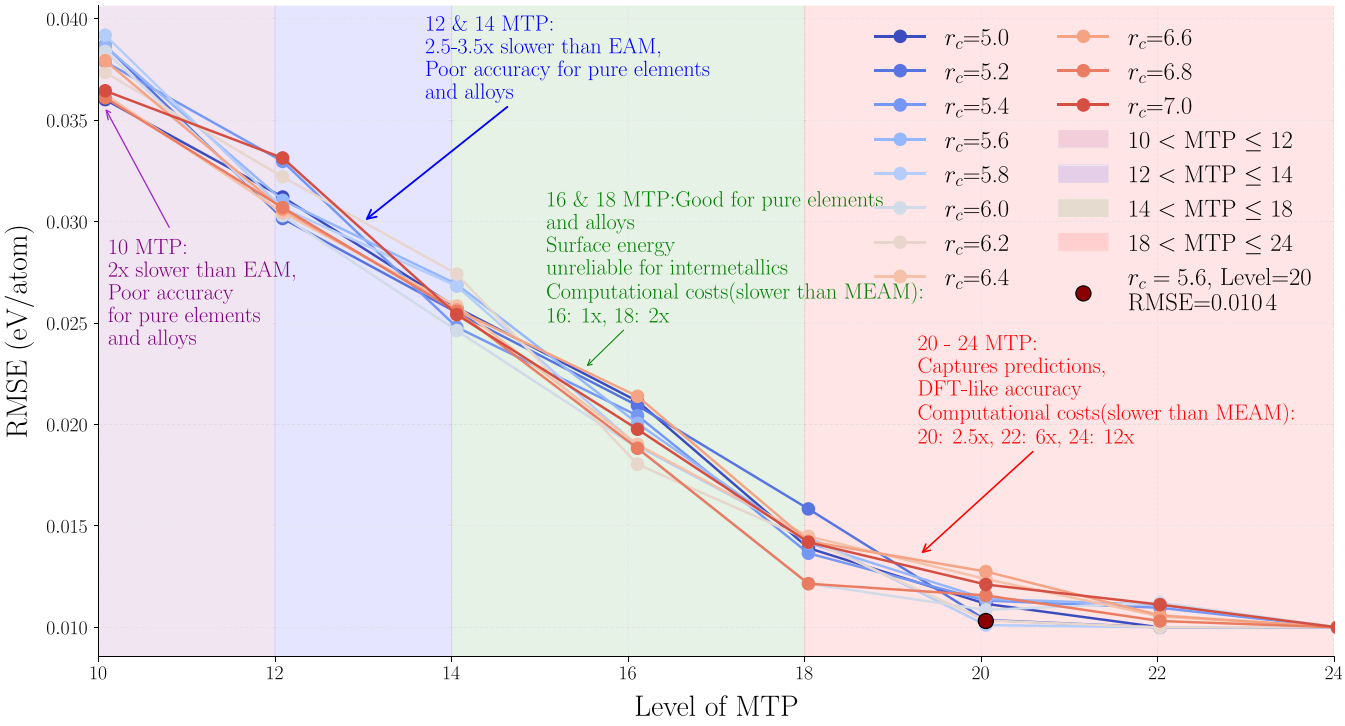

FIG. 1. Analysis of the convergence of RMSE energy per atom for various MTP potentials as a function of MTP levels and cutoff radius.

moment tensors $M_{\mu,\nu}$, defined as

$$M_{\mu,\nu}(\mathbf{n_i}) = \sum f_\mu(|\mathbf{r}_{ij}|, z_i, z_j)\, \mathbf{r}_{ij} \otimes \ldots \otimes \mathbf{r}_{ij}, \qquad (2.1)$$

where $\mathbf{n}_i$ represents the type, relative position, and neighboring atoms of the i-th atom. The position vector $\mathbf{r}_{ij}$ points from atom i to atom j, whereas z_i and z_j indicate the atomic types of the atoms and their neighbors, respectively. Radial features of the atomic environment are represented by f_μ, whereas angular information is stored by the tensor product ($\otimes$) of $\mathbf{r}_{ij}$ vectors, resulting in a rank ν tensor. The cutoff radius (r_c) and maximum level of expansion (lev_{max}) determine the balance between accuracy and computational efficiency in MTP. The cutoff radius specifies the spatial range of atomic interactions, whereas lev_{max}, an even integer typically between 2 and 28, controls model complexity by controlling the number of parameters in the moment tensor expansion. An essential component of this work is performing a grid search to optimize the MTP parameters. The search varied the potential levels from 10 to 24 and the r_c values from 5 Å to 7 Å in increments of 0.2 Å. This strategic method facilitated the examination of numerous potential configurations to identify the most successful option. For each parameter combination, 10 MTP models were trained with random initial circumstances, yielding a total of 880 models. Figure 1 shows the lowest root mean square error (RMSE) from each parameter combination among the 10 random setups. A crucial element of the convergence test involved prioritizing energy, underscoring its significant influence on the overall precision of the potential. The convergence analysis indicated that the energy per atom exhibited symptoms of convergence at level 18, except with the smallest r_c. This observation demonstrated that the MTP is able to accurately capture energy characteristics aligned with DFT estimates at this level. Levels below 16 exhibited computational speed akin to the EAM/MEAM potentials but were deficient in accuracy for unary elements. Beginning at level 16, the MTP potential demonstrated accuracy comparable to DFT values. At level 18, the MTP accurately captured most aspects, with the exception of a few errors in predicting stacking fault energy (SFE) for intermetallics. The configuration featuring level 20 MTP and $r_{\text{cut}} = 5.6$ produced the minimal RMSE and delivered DFT-accurate findings for pure Al, Ti, V, and the elastic constants of binary intermetallics, including $L1_0$.$-TiAl$ and $D0_{19}$-Ti_3Al. Higher MTP levels demonstrated comparable accuracy to level 20, although they incurred more computational costs. Figure 1 additionally shows the comparison of computational speed in relation to empirical potentials. Correspondingly, the force values exhibited markedly low RMSE commencing at level 16, reinforcing the potential's reliability from this level forward. The minimal radius (r_{min}) was established at 2.0 Å and updated during the training procedure so that the model can dynamically adapt (r_{min}) during training to better represent the pertinent short-range physics seen in the data. This adaptive approach improves the accuracy of modeling short-range forces, particularly in highly stressed structures, by guaranteeing that the potential includes all crucial interactions at small interatomic distances.

In the MTP training objective function, weights were judiciously allocated as follows: $w_e = 1$ for energy, $w_f = 0.01$ for force, and $w_s = 0.001$ for stress, emphasizing the precision of energy. This way of allocating weights ensured that force and stress were taken into account in a more complex way, though not as highly as energy, which is necessary for creating an exact interatomic potential. A 90:10 ratio of training to validation sets was used to facilitate efficient model training and subsequent validation. All MTP training,

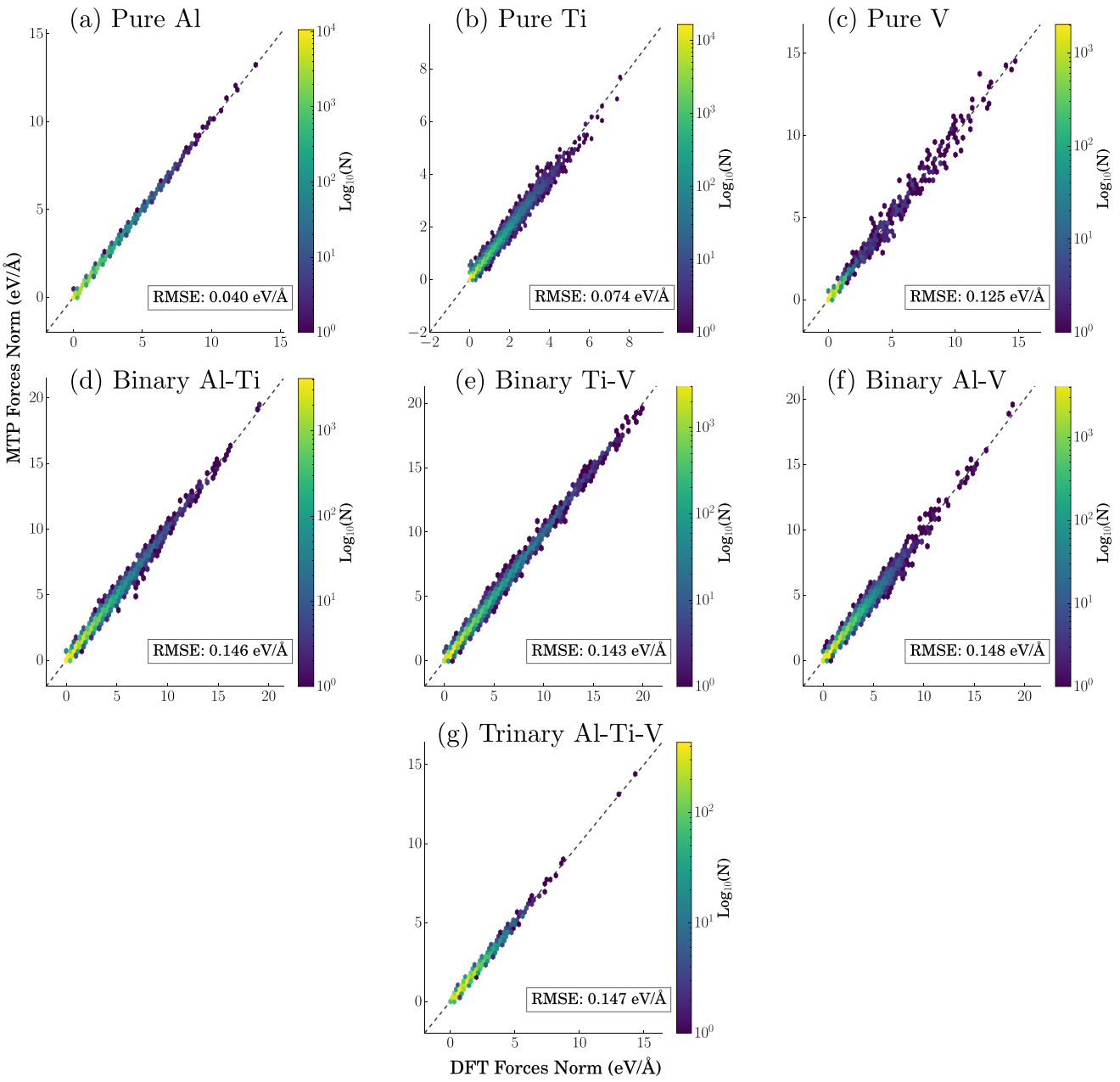

FIG. 2. Force validation of the MTP against DFT for unary, binary, and ternary Ti–Al–V. The x, y, and z components of the forces are compared for the indicated structures. The data are displayed in a hexagonal bin plot, where N represents the number of data points within each bin. The color bar shows $\log_{10}(N)$, illustrating the data density in each bin.

assessments, and simulations were conducted with MLIP [38] in LAMMPS [39] for MD simulations. The atomic trajectories and structural analysis were visualized and analyzed using the OVITO software [40], which also facilitated the generation of figures in this work.

Force validation

Forces are determined by directly differentiating the MTP, as expressed in the equation

$$\vec{f}_i = -\frac{\partial E}{\partial \vec{r}_i},$$

and evaluated in accordance with forces obtained from *ab initio* calculations. The MTP framework allows for the training of energy, force, and stress data, thus allowing the construction of a compact and efficient training database. The calculated RMSE values for forces are as follows: 0.074 eV/Å for pure Ti, 0.040 eV/Å for pure Al, 0.125 eV/Å for pure V, 0.146 eV/Å for the binary Ti-Al system, 0.143 eV/Å for the binary Ti-V system, 0.148 eV/Å for the binary Al-V system, and 0.147 eV/Å for the ternary Al-Ti-V system. The values demonstrate a significant degree of consistency between the MTP predictions and DFT results, as shown in Fig. 2, which contrasts the x, y, and z components of the forces for the specified structures.

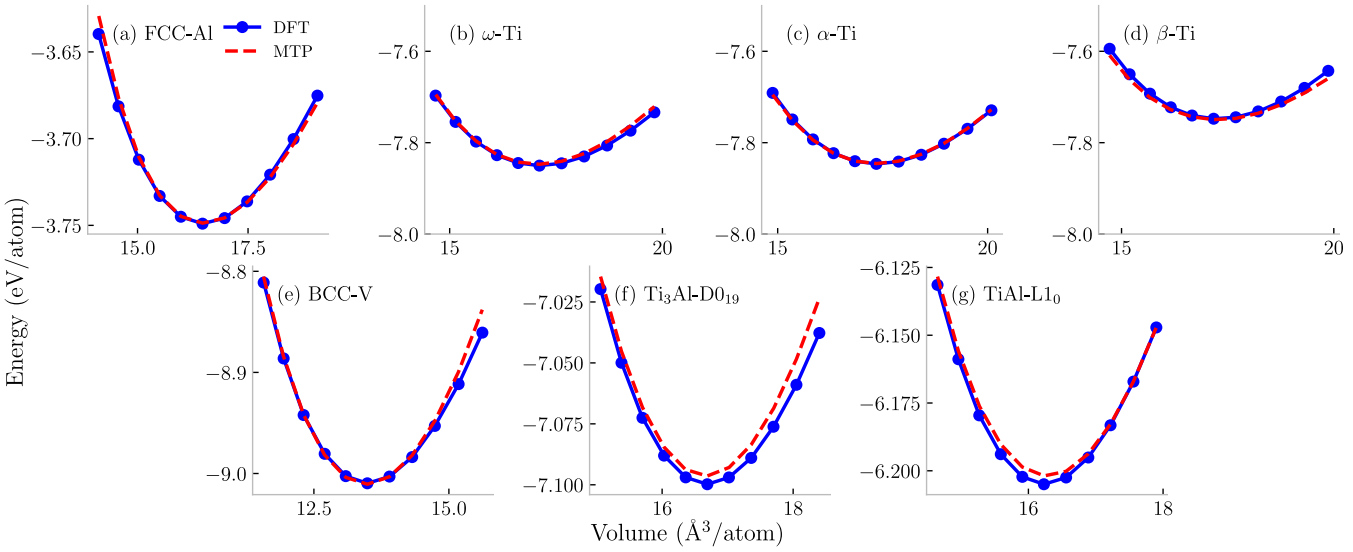

FIG. 3. The cold curves for (a) FCC-Al, (b) ω-Ti, (c) α-Ti, (d) β-Ti, (e) BCC-V, (f) Ti_3Al-$D0_{19}$, and (g) TiAl-$L1_0$ calculated by MTP and DFT.

The strong correlation between predicted and calculated forces underscores the MTP's effectiveness in precisely representing atomic-scale interactions and capturing essential short- and long-range effects. This fidelity facilitates accurate modeling of the kinetics in Al-Ti-V systems, as these forces govern dynamic processes such as diffusion, defect motion, and phase transformations.

To develop a robust potential for ternary alloys, one typically aims first for reliable accuracy in unary and binary subsystems since they serve as the fundamental building blocks of more complex compositions. In computational materials science, accurately predicted unary and binary properties establish a foundation for understanding phenomena like phase stability, defect energetics, and mechanical behavior in multicomponent alloys. Although some level of deviation in the binary subsystems can be tolerated, a reasonable baseline accuracy is still essential to ensure consistent interpolation across the entire composition space. Ultimately, the main goal is to obtain sufficient accuracy for these lower-order subsystems while prioritizing the reliable description of more intricate ternary alloy characteristics, ensuring that the overarching physics of the Al-Ti-V system is adequately captured.

III. BASIC PROPERTIES

A. Equation of state

The essential physical properties of standard phases were computed to assess the accuracy of the developed MTP Ti-Al-V model. The Ti-Al-V alloy is primarily utilized in high-temperature environments, necessitating a capability to accurately predict the α and β phases of pure Ti. This task shows significant challenges for interatomic potential development, as it is essential to accurately represent the multiphase nature of individual elements; otherwise, modeling of solid solution elements within those phases becomes impractical. Developing ML potentials for intermetallic compounds is relatively straightforward, as the training database primarily targets specific formed phases. In the context of a multiphase solid solution, the training database necessitates considerable expansion, alongside the need to address additional complexities. Consequently, the accurate prediction of the properties of individual elements using the current MTP potential is considered crucial.

Figure 3 shows the cold curves for various structures, including FCC-Al, ω-Ti, α-Ti, β-Ti, BCC-V, Ti_3Al-$D0_{19}$, and TiAl-$L1_0$. For all structures, there is excellent agreement between the equation of state (EOS) curves by MTP and DFT throughout the entire volume range studied, which corresponds to a volumetric strain of $\pm 10\%$. The RMSE between MTP and DFT is under 1.2 meV/atom. Accurate cold curves are essential for predicting mechanical behavior across a broad spectrum of volumetric strains and pressures.

The physical properties, encompassing lattice parameters $(a, c, c/a)$, equilibrium volume (V_0), and energy differences (ΔE), are given in Table I for pure metals and binary systems. DFT calculations and available experimental data are provided as reference values. The precision of the MTP model is measured by the absolute value of the relative error compared to experimental data or DFT results when experimental values are not accessible. The MTP model exhibits significant concordance with reference values, accurately replicating lattice parameters, equilibrium volumes, and energy differentials between phases for both elemental and binary systems. This degree of precision underscores MTP's durability and adaptability.

The physical properties, including lattice parameters $(a, c, c/a)$, equilibrium volume (V_0), and energy differences (ΔE), are presented in Table I for pure metals and binary systems. Corresponding DFT calculations and available experimental data are included as references. The accuracy of the MTP model is quantified by the absolute value of the relative error with respect to experimental data or DFT results when experimental values are unavailable.

The MTP model demonstrates remarkable agreement with reference values, effectively reproducing lattice constants,

TABLE I. Lattice parameters a (Å), c (Å), equilibrium volume per atom V_0 (Å^3/atom), and energy differences ΔE (meV/atom) for unary and binary structures in the Ti-Al-V alloy system.

Properties	Expt.	DFT	MTP	Properties	Expt.	DFT	MTP
	FCC-Al				α-Ti		
a	4.05 [41]	4.04	4.04	a	2.95 [42]	2.94	2.93
V_0		16.48	16.48	c	4.67 [42]	4.65	4.66
$\Delta E_{fcc\to bcc}$		97.17	74.19	V_0		17.36	17.35
$\Delta E_{fcc\to hcp}$		32	8	$\Delta E_{hcp\to fcc}$		58	46
$\Delta E_{fcc\to sc}$		366	293	$\Delta E_{hcp\to bcc}$		107	96
$\Delta E_{fcc\to \omega}$		114	90	$\Delta E_{hcp\to sc}$		821	451
$\Delta E_{fcc\to a15}$		76	92	$\Delta E_{hcp\to \omega}$		−3	−2
$\Delta E_{fcc\to \beta Sn}$		274	220	$\Delta E_{hcp\to a15}$		192	63
	β-Ti				ω-Ti		
a		3.25	3.26	a		4.58	4.57
V_0		17.17	17.27	c		2.83	2.83
	BCC-V			V_0		17.11	17.06
a	3.03 [42]	3.00	3.00		$D0_{19}$-Ti_3Al		
V_0		13.49	13.48	a	5.77 [43]	5.76	5.75
$\Delta E_{bcc\to fcc}$		243	188	c	4.62 [43]	4.65	4.65
$\Delta E_{bcc\to hcp}$		250	181	V_0		16.69	16.66
$\Delta E_{bcc\to sc}$		840	435		$L1_0$-TiAl		
$\Delta E_{bcc\to \omega}$		134	105	a	2.82 [44]	2.83	2.84
$\Delta E_{bcc\to a15}$		56	117	c	4.06 [44]	4.06	4.02
$\Delta E_{bcc\to \beta Sn}$		478	381	V_0		16.24	16.25

equilibrium volumes, and energy differences for both elemental and binary systems. This level of accuracy is particularly noteworthy given that the MTP potential was trained across unary, binary, and ternary combinations, highlighting its robustness and versatility.

Figure 4 shows the formation energies of specific ordered structures as estimated by the MTP alongside those computed by DFT for both Ti-Al and Ti-V alloys. It is essential to recognize that these ordered structures include a wide variety of compositions. For Ti-Al, both MTP and DFT indicate that the $D0_{19}$ and $L1_0$ structures are low-energy configurations as the Al concentration increases. To appropriately simulate the Ti-Al system, the potential must demonstrate that Al is soluble in Ti. DFT indicates that the substitutional energy of Al in Ti for the stable α phase is −889 meV. MTP indicates an energy of −929 meV; thus, MTP correctly predicts the solubility of Al in Ti. As demonstrated in Fig. 4, the formation energies for Ti-V, as predicted by both DFT and MTP for all examined ordered structures, are positive, signifying that none of these ordered phases are stable within the Ti-V system.

B. Elastic properties

Table II presents the stiffness tensor (C_{ij} values) calculated using DFT and MTP for a range of structures, including FCC-Al, BCC-V, ω-Ti, α-Ti, β-Ti, $D0_{19}$-Ti_3Al, and $L1_0$-TiAl. MTP values are accompanied by the absolute percentage errors relative to DFT, providing a quantitative measure of the potential's accuracy. For FCC-Al, the MTP potential exhibits excellent agreement with DFT, with percentage errors below 0.3% for C_{11}, though slightly larger deviations are observed for C_{12} and C_{44}. Similarly, for BCC-V and ω-Ti, MTP captures the elastic properties with a high degree of accuracy, with most errors falling within ±5%. Notably, larger deviations are observed for certain constants, such as C_{13} in ω-Ti, where the error reaches 23.39%. The intermetallic systems $D0_{19}$-Ti_3Al and $L1_0$-TiAl also demonstrate strong consistency between MTP and DFT, with errors generally within 10%. The MTP model correctly replicates the negative Cauchy pressure $C_{13} - C_{44} = -16$ GPa for $L1_0$-TiAl, which is comparable to the DFT value of −21 GPa. The empirical EAM potentials fail to capture the negative Cauchy pressures ($C_{13} - C_{44} = -34$ GPa and $C_{12} - C_{66} = -6.4$ GPa) in $L1_0$-TiAl as observed experimentally. Instead, both EAM and MEAM potentials predict positive Cauchy pressures ($C_{12} - C_{66} = 22$ [45], 45 [46], 14 [47]; $C_{13} - C_{44} = 22$ [45], 44 [46], 48 [47]) and exhibit anomalously negative SFEs on the pyramidal planes of the $D0_{19}$-Ti_3Al structure [48]. Overall, the MTP potential demonstrates robust predictive capabilities, capturing the elastic properties of complex unary, binary, and intermetallic systems with reasonable accuracy, making it a powerful tool for the Ti-Al-V alloy. Training the model exclusively on individual elements should yield more accuracy in predicting 0 K elastic constants. In the meantime, the inclusion of multielements may lead to a degradation of a few properties, as evidenced in other ML potentials [49].

C. Phonon dispersion

Figure 5 compares the phonon spectra of FCC Al, three phases of Ti, BCC V, and the $L1_0$ phase of TiAl, as obtained from DFT and MTP. The phonon dispersion along high-symmetry directions in the Brillouin zone was calculated

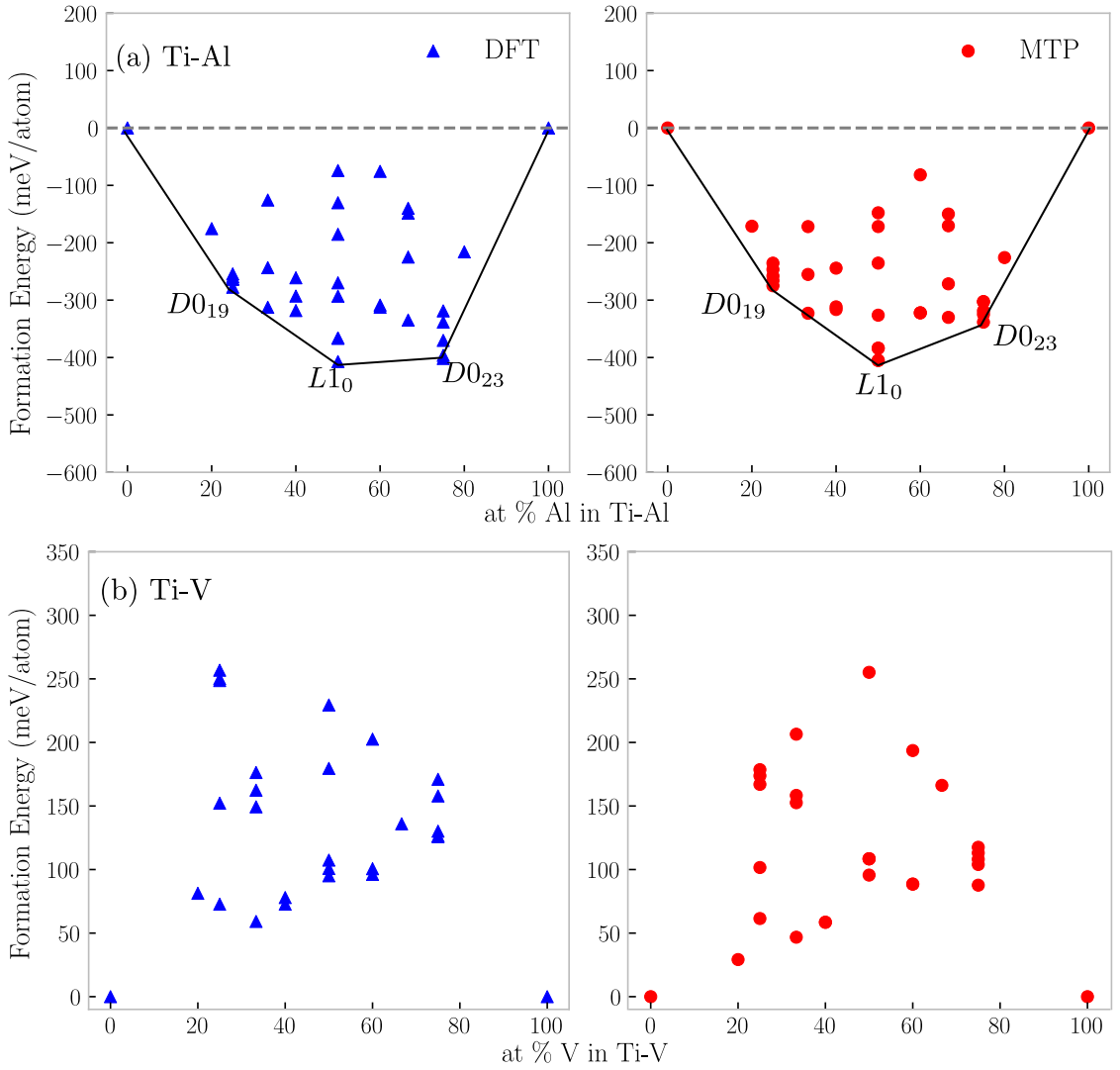

FIG. 4. Formation energy of various ordered structures as predicted by DFT and MTP for both (a) Ti-Al and (b) Ti-V alloys.

TABLE II. Elastic properties (C_{ij} values) calculated using DFT and MTP potentials for various structures. Percentage errors of MTP relative to DFT are shown in parentheses.

Structure	Property	Expt.	DFT	MTP (Error %)	Structure	Property	Expt.	DFT	MTP (Error %)
FCC-Al	C_{11}	114.3 [50]	109.35	109.66 (0.28%)	BCC-V	C_{11}	232.4 [51]	261.60	258.83 (1.06%)
	C_{12}	61.9 [50]	63.78	56.69 (11.12%)		C_{12}	119.4 [51]	144.56	151.70 (4.94%)
	C_{44}	31.6 [50]	32.90	38.41 (16.74%)		C_{44}	46.0 [51]	23.61	33.81 (43.23%)
ω-Ti	C_{11}		194.07	184.17 (5.10%)	$D0_{19}$-Ti_3Al	C_{11}	183 [52]	195.44	196.24 (0.41%)
	C_{12}		84.99	95.63 (12.50%)		C_{12}	89 [52]	90.07	103.16 (14.53%)
	C_{13}		54.95	67.82 (23.39%)		C_{13}	63 [52]	67.08	63.01 (6.07%)
	C_{33}		245.20	235.01 (4.16%)		C_{33}	225 [52]	223.29	217.81 (2.46%)
	C_{44}		54.32	55.64 (2.43%)		C_{44}	64 [52]	59.28	53.95 (8.99%)
α-Ti	C_{11}	176.1 [53]	171.42	169.55 (1.09%)		$C_{13}-C_{44}$	−1 [52]	7.80	9.06 (16.15%)
	C_{12}	86.9 [53]	93.22	92.96 (0.28%)	$L1_0$-TiAl	C_{11}		200.98	193.10 (3.91%)
	C_{13}	68.3 [53]	74.67	66.56 (10.86%)		C_{12}		61.99	49.28 (20.52%)
	C_{33}	190.5 [53]	197.25	201.32 (2.06%)		C_{13}		90.21	98.27 (8.94%)
	C_{44}	50.8 [53]	42.47	35.46 (16.49%)		C_{33}		164.55	150.89 (8.31%)
β-Ti	C_{11}	134 [53]	89.78	87.19 (2.88%)		C_{44}		111.13	113.78 (2.38%)
	C_{12}	110 [53]	110.90	98.39 (11.28%)		$C_{13}-C_{44}$		−20.93	−15.51 (25.91%)
	C_{44}	36 [53]	42.40	42.27 (0.31%)					

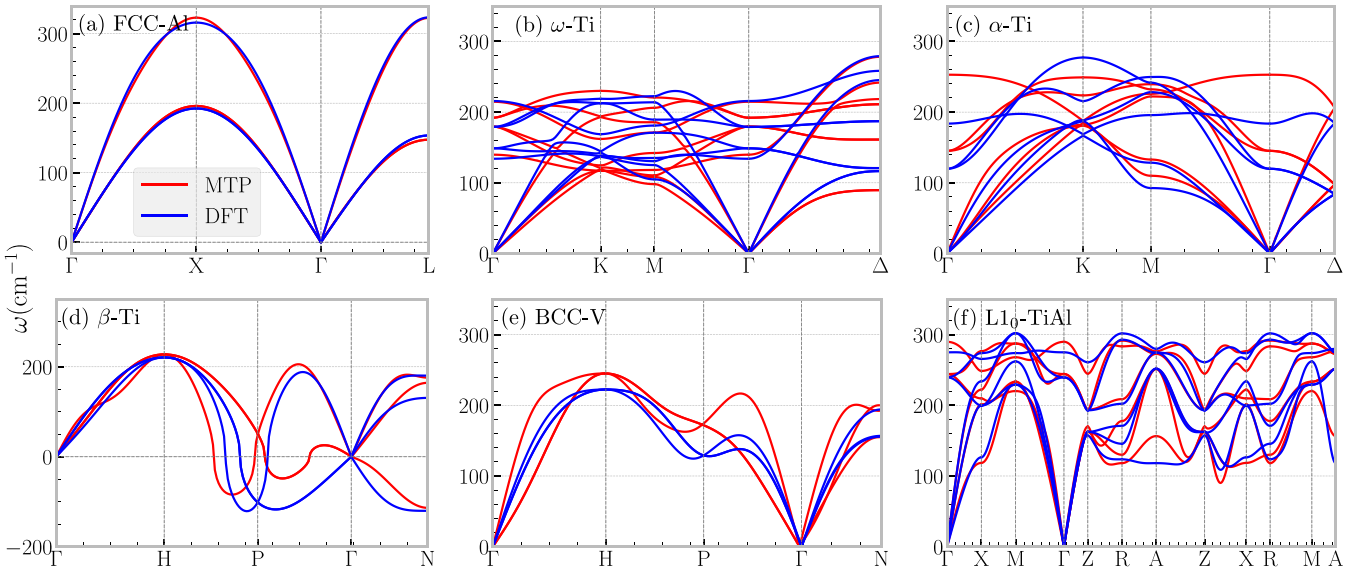

FIG. 5. Phonon spectra curves for (a) FCC-Al, (b) ω-Ti, (c) α-Ti, (d) β-Ti, (e) BCC-V, and (f) $L1_0$-TiAl, as calculated using both DFT and MTP.

utilizing the PHONOPY [54] package through the finite-displacement approach. The MTP potential exhibits strong agreement with phonons calculated using DFT, replicating them with an accuracy of roughly 8%. The force-matching technique and the fitting of elastic constants utilized in the model contribute to the exceptional accuracy. The acoustic branches are more precisely represented than the optical modes, indicating the accuracy of the elastic constants employed in the fitting procedure.

The β phase exhibits mechanical instability at reduced temperatures, as indicated by the soft mode detected in experimental phonon data along $L - \frac{2}{3}[111]$ [55]. The MTP accurately replicates this soft mode, whereas the empirical potentials do not [45,56], precluding the replication of the $\beta \rightarrow \omega$ Ti transformation. In more intricate binary TiAl systems, the phonon dispersions forecasted by the MTP are substantially aligned with DFT results. Though intermetallics like Ti_3Al and TiAl are taken into consideration, it should be emphasized that the current potential is trained toward the Ti6Al4V alloy. For example, it does not consider compositions like Ti48Al alloy, and so may not be able to fully capture its behavior. Nonetheless, the MTP attains DFT-level precision for these intermetallics, illustrating its robustness.

D. Surface and defect properties

Table III presents the low-index surface energies and vacancy formation energies for various subsystems in the Ti-Al-V alloy system. The MTP model enables precise calculations of surface energies for elemental structures, demonstrating errors of less than 5% in comparison to DFT values. The vacancy formation energy (E_{vf}) obtained from the MTP model shows a strong correlation with DFT data. In traditional binary Ti-Al systems, surface energies calculated with the MTP model exhibit a 2.6% error margin in comparison to DFT values, demonstrating enhanced accuracy relative to classical potentials. The decohesion behavior, which reflects the rigid separation of two semi-infinite blocks of a perfect crystal perpendicular to the surface of interest, is illustrated in Fig. S1 of the Supplemental Material [62] and is accurately represented by the MTP across all examined surfaces. The precise replication of both properties is crucial for the effective application to fracture problems, though this alone is not sufficient.

E. Solute effects on generalized stacking fault energies (GSFEs) in Ti alloys

Following previous studies by Nitol *et al.* [63] and Kwasniak *et al.* [64], the effects of solute elements in pure Ti were

TABLE III. Comparison of defect properties between Expt, DFT, and MTP for various structures. All surface energies (E_*) are in units of mJ/m^2 and monovacancy formation energy (E_{vf}) is in eV.

Structure	Property	Expt.	DFT	MTP
FCC-Al	E_{100}	Polycrystalline	874	873
	E_{110}	surface energy	962	976
	E_{111}	1085 [57]	810	811
	E_{vf}	0.68 [58]	0.64	0.61
α-Ti	E_{0001}	2100 [59]	1938	1886
	E_{1010}	1920 [60]	2451	2490
	E_{1011}		1948	1872
	E_{1121}		2141	2181
	E_{vf}	1.50 [59]	2.06	2.69
BCC-V	E_{100}	Polycrystalline	2572	2702
	E_{110}	surface energy	2438	2602
	E_{112}	2876 [57]	2869	2906
	E_{vf}	2.10 [61]	2.6	2.25
Ti_3Al	E_{0001}		1938	1875
TiAl	E_{111}		1667	1713

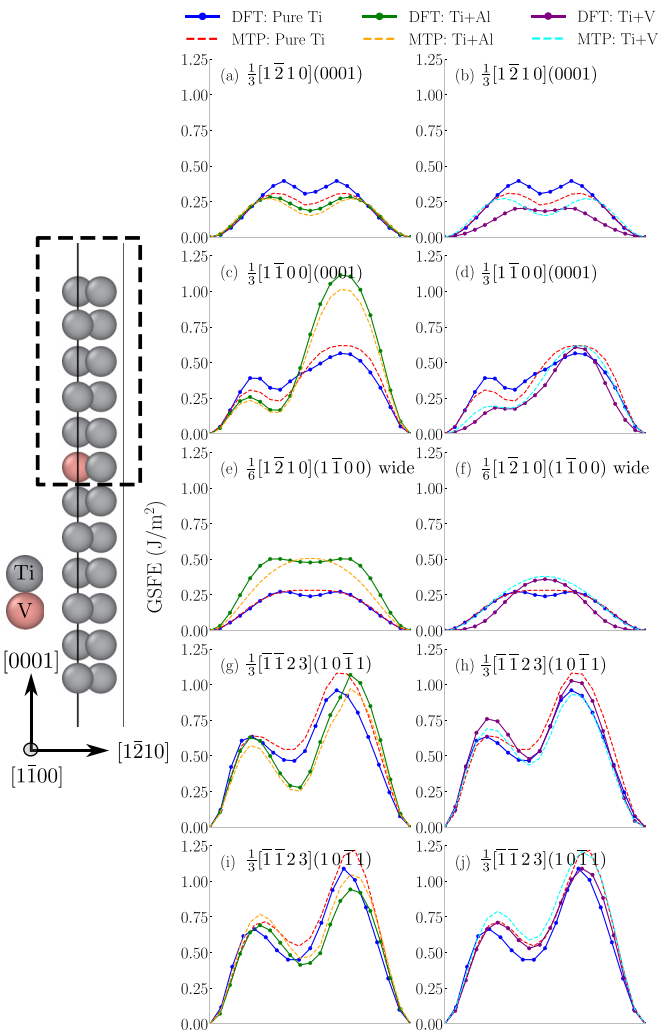

FIG. 6. (Left) A schematic illustrates the position of the solute atom within the prismatic fault plane, where half of the simulation box was sheared along the $\langle a \rangle$ direction to compute GSFE. (Right) GSFE curves for α-Ti, α-TiAl, and α-TiV alloys across basal, prismatic, pyramidal I, and pyramidal II planes.

examined, as shown in Fig. 6, with the solute atom positioned at the slip plane. The addition of Al and V was found to significantly modify the dislocation behavior and GSFE landscape of α-Ti, thereby enhancing its mechanical strength. Although the mechanisms differed, both solutes contributed to strengthening.

Al, a p-type solute, was observed to strengthen α-Ti notably by impeding the emission of prismatic dislocations, thereby increasing resistance to plastic deformation. The nonplanar core of screw dislocations ($\frac{1}{2}\langle 1\,1\,\bar{2}\,0\rangle$) was stabilized, leading to reduced dislocation mobility. A dual effect on SFE was observed: A reduction in basal SFE promoted stabilization of less mobile dislocation core configurations, while an increase in prismatic SFE facilitated planar slip, enhancing the material's overall strength. As a result, Al's effect on both fault stability and slip resistance was substantial.

V, a d-type solute, exhibited a moderate strengthening effect. Prismatic dislocation emission was hindered, though less effectively than in the case of Al. A reduction in SFEs, particularly for prismatic and pyramidal slip systems, was observed, which was associated with localized lattice distortions. However, the stabilization of dislocation cores was not achieved to the same extent as with Al, resulting in a comparatively lower strengthening impact.

These observations underscore the distinct roles of Al and V in the solid solution strengthening of α-Ti, with Al producing a more pronounced effect due to its electronic structure and stronger influence on dislocation stabilization and GSFE modification.

Additional GSFE calculations were performed for various crystallographic planes in Ti-Al intermetallic phases, as shown in Fig. 7. In the $D0_{19}$ phase, basal, pyramidal I, pyramidal II, prismatic narrow, prismatic wide I, and prismatic wide II planes were considered, while the (1 1 1) plane was used for the $L1_0$ phase. The MTP demonstrated excellent agreement with reference data for predicting GSFE in these intermetallics, consistent with previous studies trained on Ti-Al systems [29]. For additional discussion of slip systems and crystallographic directions, readers are referred to Ref. [29].

IV. APPLICATION OF THE MTP MODEL

A. Phase stability in Ti, Ti-Al, and Ti-V alloys

1. Pure Ti

MTP is used to investigate phase stability in the Ti-Al-V system and subsystems through the following steps: (a) evaluate the potential for predicting multiphase stability in Ti; (b) assess phase stability within the binary Ti-Al phase diagram; and (c) analyze phase stability in the binary Ti-V phase diagram. Ti experiences a diffusionless transformation from HCP to BCC structure at 1155 K [65] under ambient pressure conditions; meanwhile, it transitions to a hexagonal ω phase at approximately 2 GPa at room temperature [66]. Phase transformations in pure Ti are essential for comprehending phase stability in Ti-based alloys.

Although MD simulations can capture phase transformation pathways, interface motion mechanisms, and transformation rates, they face significant challenges in establishing equilibrium phase transformation boundaries. Specifically, if the barrier to transformation is large, the system may not spontaneously overcome this barrier within accessible simulation timescales, which can obscure or delay the emergence of equilibrium transitions [67]. Consequently, MD simulations alone may not suffice to pinpoint the thermodynamic phase transition with high precision, even though they can provide detailed insights into the transformation mechanisms once a phase change is underway. Hence, equilibrium phase diagrams are determined by calculating the relative Gibbs free energy of phases as a function of temperature and pressure in MD simulations. The equilibrium phase transition point is identified by observing the change in the sign of the free energy [68]. The temperature dependence of free energy is assessed through the Gibbs-Helmholtz equation $\frac{\partial(\frac{G}{T})}{\partial T}|_p = -\frac{H}{T^2}$, which incorporates G as the Gibbs free energy, T as the temperature, p as the pressure, and H as the enthalpy.

Based on prior research [34], the transition temperature from α-Ti to β-Ti is known. Figure 8 shows the relative Gibbs free energy at zero pressure, where a sign change in ΔG

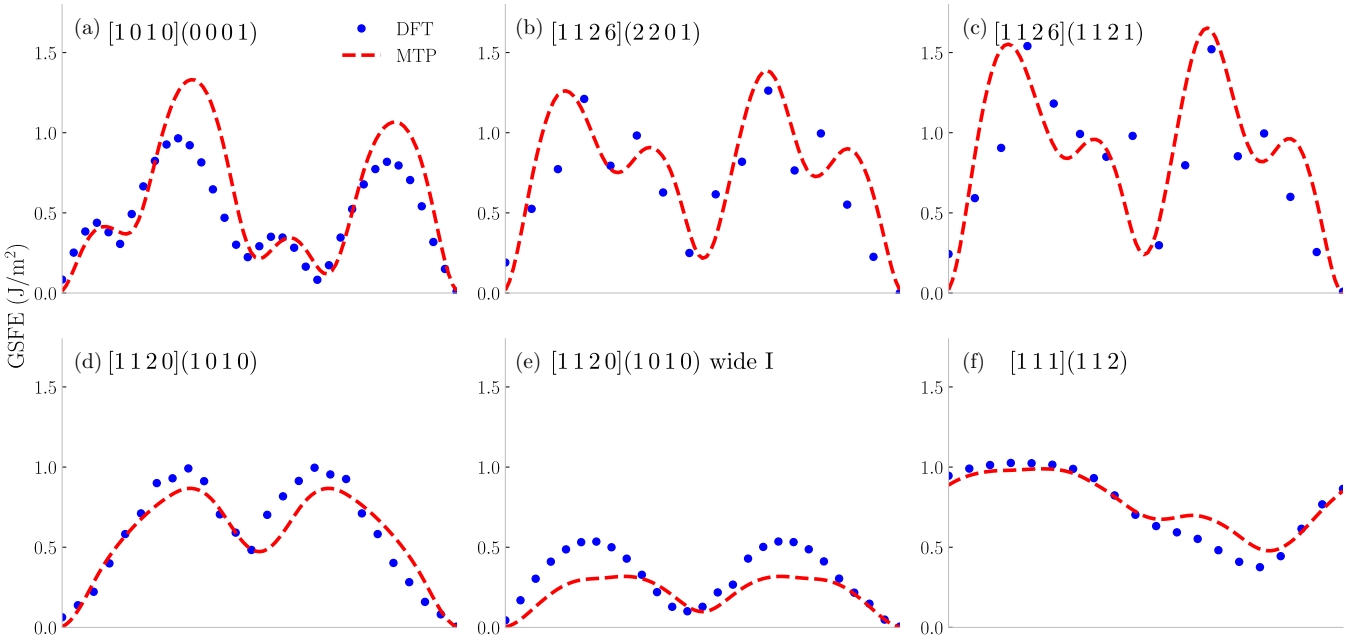

FIG. 7. GSFE curves for (a) basal, (b) pyramidal I, (c) pyramidal II, (d) prismatic wide I, and (e) prismatic wide II planes in the $D0_{19}$ Ti_3Al phase and (f) the (1 1 1) plane in the $L1_0$ TiAl phase.

signifies an equilibrium phase transition. The phase diagrams illustrated in Fig. 8 align with the experimental data. The zero-pressure $\alpha \rightarrow \beta$ transition is predicted to occur at 1083.3 K, while the experimentally observed value is 1155 K [65], resulting in an error of 6.0%. Using the same methodology at constant temperature 300 K, as the pressure rises, the phase transformations in Ti are predicted to occur at about 2.1 GPa, aligning well with experimental measurements of 2 ± 0.3 GPa [69].

2. Ti-Al

Accurately modeling the Ti-Al system with varying concentrations of Al is essential. A potential must accurately represent essential material properties across varying Al concentrations and predict the temperatures or Al concentrations at which phase transitions occur. The MTP potential accurately replicates the phase diagram for Al concentrations up to 25%. The α-to-D019 transition is modeled through the semi-grand-canonical Monte Carlo (SGCMC) method [47] as implemented in LAMMPS. This method initiates with pure α-Ti equilibrated at a specified temperature and a defined chemical potential value (μ).

The SGCMC fix in LAMMPS utilizes the Metropolis acceptance criterion [70], which includes a term for the chemical potential difference, $\Delta\mu$. At each MD timestep, the algorithm performs 10 attempts to swap a Ti atom with an Al atom, accepting the swap according to the Metropolis algorithm [71]. Simulations involving 2048 atoms of the αphase were performed at different temperatures for 100 ps. The identical procedure was implemented for the $D0_{19}$ structure. The atomic percentage of Al at which the α phase transitions to the $D0_{19}$ phase marks the transition point. As the Al composition changes, the system eventually switches from the α phase to the $D0_{19}$ phase. Conversely, when Al composition is reduced from a $D0_{19}$-stabilizing level, there is a point where $D0_{19}$ can no longer be maintained, causing the system to revert to the α phase. This final Al fraction at which the $D0_{19}$ phase persists just before reverting is taken as the transition from $D0_{19}$ to α. In other words, it marks the maximum Al composition at which $D0_{19}$ remains stable before the system re-enters the α-phase regime.

The phase transition predicted by the MTP model is in close agreement with results from CALPHAD and Nichols *et al.* [24]. Simulations were performed at temperatures of 900 K, 1000 K, 1100 K, and 1200 K, respectively. Figure 9 presents the hysteresis loops at temperatures of 900 K and 1000 K. The outcome of MTP potential indicates that the α-to-$\alpha + D0_{19}$ phase boundary is observed at Al concentrations of 8.5%, 10.45%, 14.12%, and 18.16% at temperatures of 900 K, 1000 K, 1100 K, and 1200 K, respectively. The $D0_{19}$-to-$\alpha + D0_{19}$ phase boundary is predicted at Al concentrations of 24.7%, 24.69%, 24.23%, and 25.04% for the corresponding temperatures.

The capacity to model phase transitions is crucial, given that numerous commercially utilized Ti-Al-V alloys consist of α and β phases. Figure 9 also shows the transition temperatures for Al concentrations varying from 0% to 20% in increments of 2%. SGCMC/MD simulations were utilized to position Al atoms in their preferred lattice sites within Al-containing structures.

To evaluate the thermodynamic stability, the Gibbs free energy differences between competing phases were computed. These calculations were performed at fixed chemical compositions for Ti–Al alloys with 2 to 20% Al. For each composition, the vibrational contributions to the enthalpy were obtained using temperature-dependent molecular dynamics simulations. Configurational degrees of freedom were not sampled during these calculations, and hence configurational entropy and correlation effects were not explicitly

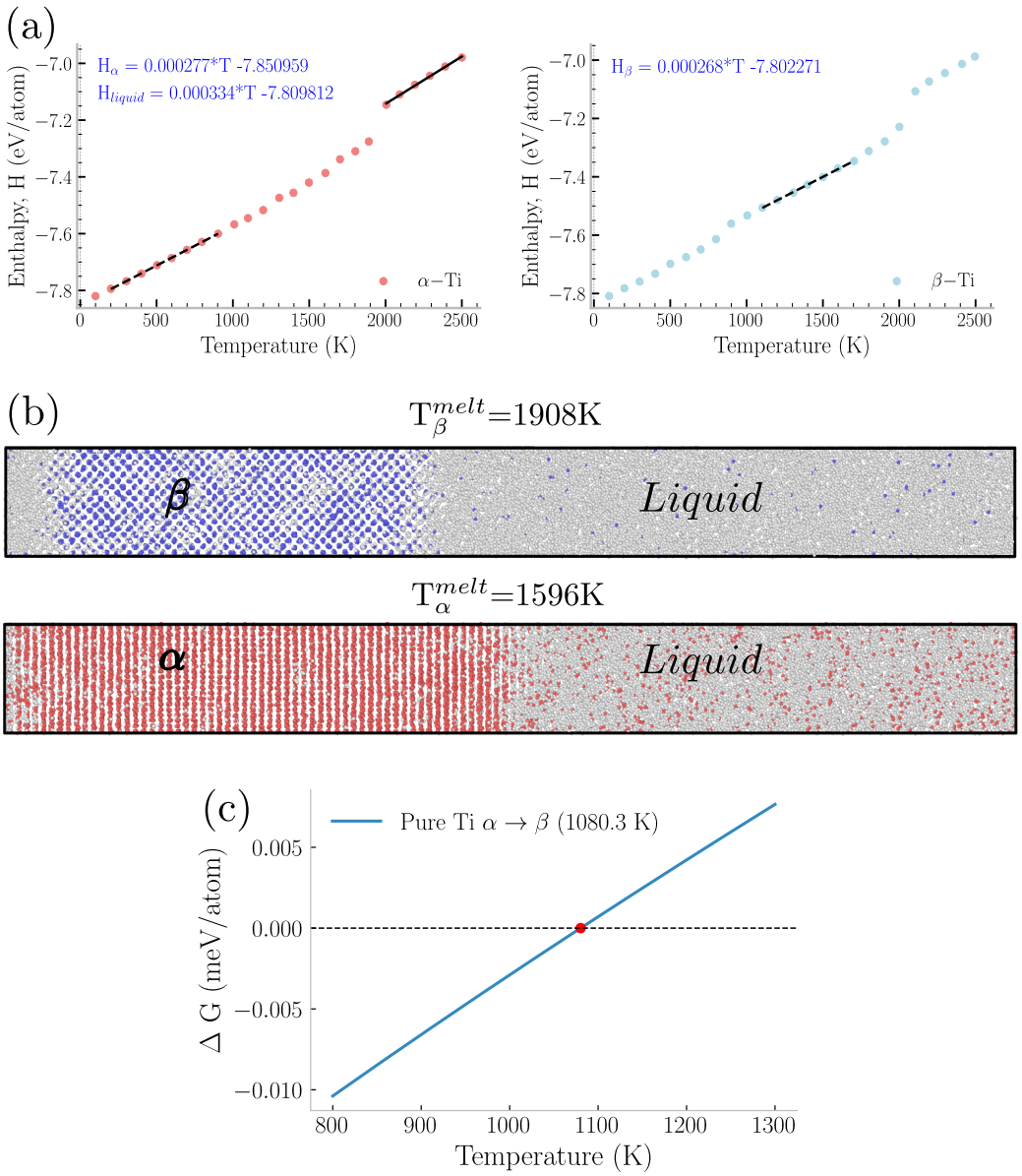

FIG. 8. (a) Enthalpy as a function of temperature for α-Ti and β-Ti, including their respective fitting equations for both solid and liquid phases. (b) Calculation of the melting point based on the two-phase region for α-Ti and β-Ti. (c) Gibbs free energy analysis to determine the transition temperature from α-Ti to β-Ti.

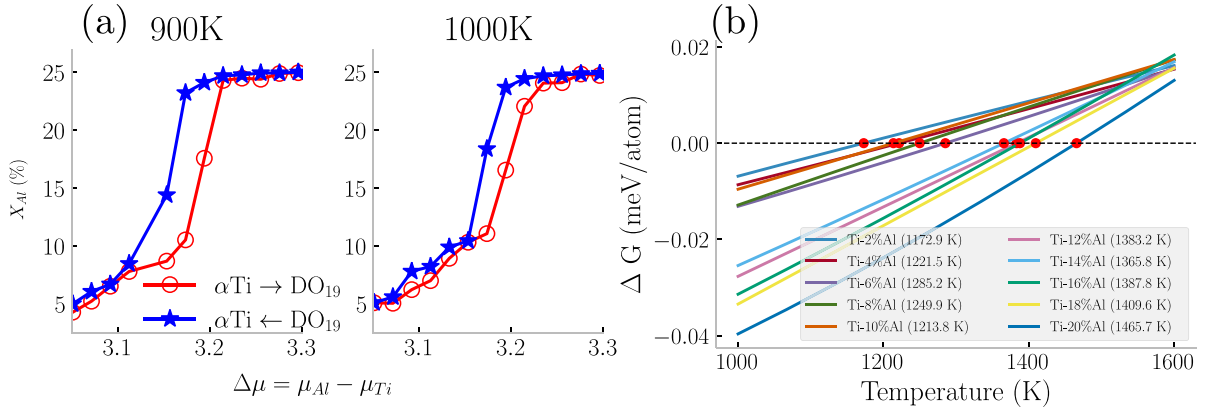

FIG. 9. (a) Hysteresis loop obtained from SGCMC simulations of the Ti–Al alloy at 900 K and 1000 K. (b) Gibbs free energy calculations for the Ti–Al alloy with Al concentrations ranging from 2% to 20% in 2% increments.

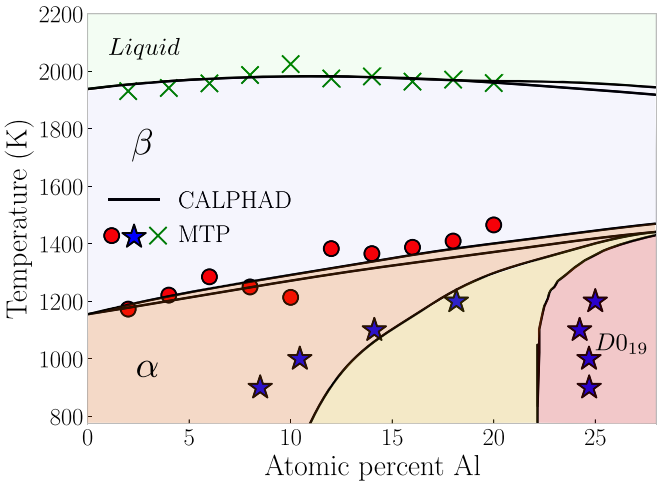

FIG. 10. Phase diagram of the Ti-Al binary system predicted by the MTP model, compared with CALPHAD results. The markers show the MTP-calculated transition temperatures as a function of the atomic percentage of Al: the star (★) denotes the transition between α-Ti and $D0_{19}$, the circle (●) denotes the transition between α-TiAl and β-TiAl, and the cross (×) denotes the transition between β-TiAl and the liquid phase.

included in ΔG. This approach provides a vibrationally resolved but compositionally constrained view of the relative phase stability.

The melting points of β-Ti with Al concentrations ranging from 2% to 20% (in 2% increments) are as follows: 1931 K, 1942 K, 1958 K, 1987 K, 2025 K, 1975 K, 1982 K, 1964 K, 1971 K, and 1959 K, respectively. A similar trend of melting point was observed experimentally by Witusiewicz *et al.* [72]. The phase boundaries predicted by the MTP potential are shown in Fig. 10. The MTP developed by Qi *et al.* [29] demonstrates strong performance in predicting basic and plastic properties of intermetallic structures; however, its accuracy decreases for solid solutions. The improved MTP here, developed using a ternary database, exhibits similar performance for intermetallics and solid solutions for binary alloys, too.

3. Ti-V

In Ti-V, the stability of phases was evaluated through a hybrid simulation approach combining MC and MD methods, outlined as follows: The initial configuration was a bulk α-Ti simulation box containing 10 976 atoms, generated by replicating a four-atom conventional unit cell in a $14 \times 14 \times 14$ grid. To achieve the target composition, some Ti atoms were replaced with V atoms randomly. The system was first equilibrated using an NPT ensemble for 5 ps under zero pressure and at a specified temperature. Subsequently, MC swaps of Ti and V atoms were performed at the same temperature, with the Metropolis criterion used to determine whether each swap takes place. Throughout the simulation, the NPT thermostat consistently integrated atomic displacements over time. Ten MC swaps were attempted at each step, followed by MD simulations lasting 2 nanoseconds. To ensure robustness and minimize dependency on random seed selection, each MC + MD simulation was repeated three times with different seeds.

By performing simulations over a range of temperatures and compositions, metastable regions for the α, β, and ω phases were identified. As illustrated in Fig. 11, MTP effectively captures the occurrence and transitions of phases in the alloy. This adaptability enables enhanced predictions of material behavior, providing deeper insights into atomic transformations and interactions through data-driven learning.

Below the α/β transition temperature, the system stabilizes into the $\alpha + \beta$ phase, a result that aligns with earlier DFT-based MC studies [73]. Small β-phase precipitates are predicted to form due to the low solubility of V in α-Ti, promoting phase separation and stabilization of the $\alpha + \beta$ two-phase region. Nearly complete segregation occurs, with Ti concentrating in the α phase and V preferring the β phase, reflecting the limited solubility of V in α-Ti. This two-phase region is consistent with experimental data [74–77].

With an increasing temperature, phase transitions proceed from $\alpha + \beta$ to α, then to β, and finally to $\beta + \omega$. For V concentrations of approximately 14 to 22 at.% within a temperature range of 200 to 900 K, a $\beta + \omega$ two-phase region emerges as shown in Fig. 12. Segregation is again pronounced, with the ω phase exhibiting minimal V content. Similar stability for the $\beta + \omega$ region has been reported experimentally by [77]. The prediction of the metastable ω phase by the MTP is particularly significant, as this phase, interacting with β grains, is likely to serve as a nucleation site for the formation of stable α-Ti [74]. The results of all MC + MD analyses are displayed in Fig. 12. The available experimental data are also included for reference. For information on the stability of the $\alpha + \beta$ phase based on DFT, readers are referred to Ref. [73].

B. Phase stability in the Ti-6Al-V alloy system

Since the current MTP model successfully predicts phase stability in Ti, Ti-Al, and Ti-V systems, it is reasonable to expect similar predictive performance for Ti-6Al-V alloys. To perform MC + MD simulations as described above, varying concentrations of V are added to an α-Ti6Al matrix. Like Ti-V alloys stated before, the simulation box size and process parameters are set to the same values. For example, in the exact stoichiometry of the Ti-6Al-4V alloy, the minor alloying components include 10.2% Al and 3.6% V by number. When the V concentration exceeds 6% in the Ti6Al matrix, β-phase precipitates form within the α-Ti6Al alloy. With a subsequent temperature increase, these precipitates first transform into α phase and later revert to β phase in the Ti6Al matrix. Figure 13 illustrates the predicted phase stability derived from MC + MD simulations using the MTP model. Despite the training database containing only DFT data for random alloys without any DFT MC data, the current MTP framework accurately captures phase stability in these multiphase short-range ordering systems.

V. CONCLUSION

This study demonstrates the successful development and application of an MLIP for the Ti-Al-V ternary system, enabling high-fidelity atomistic simulations of phase stability and microstructural evolution. This potential establishes a new paradigm for Ti alloy design, providing researchers

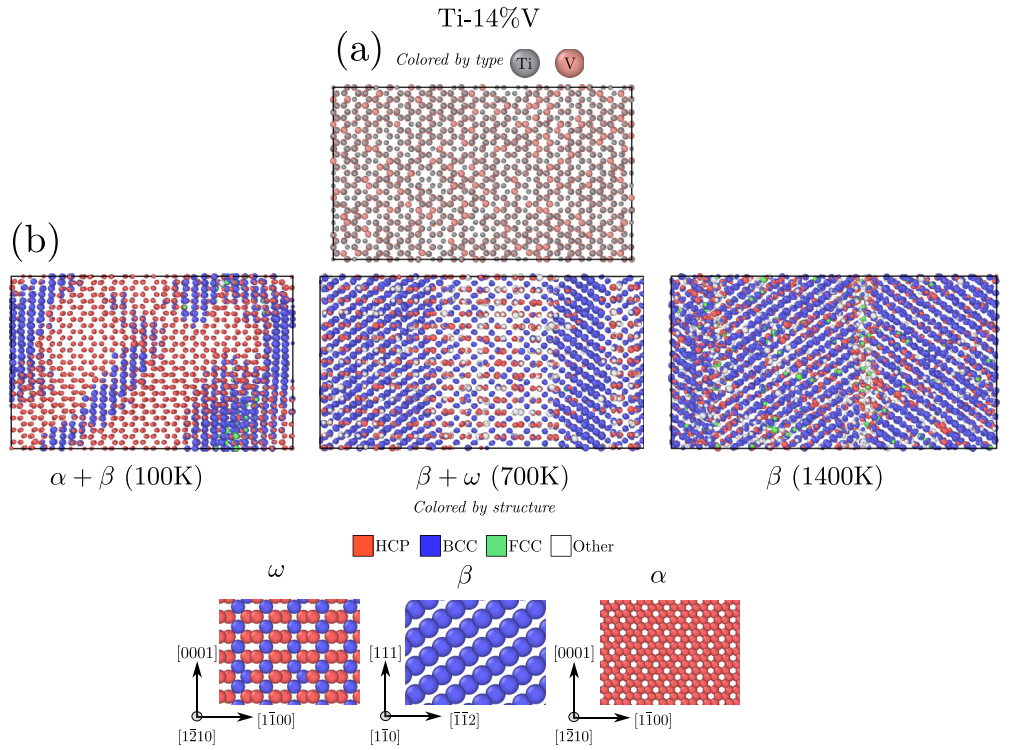

FIG. 11. (a) The initial random structure of Ti-14%V, with atoms colored by their types. (b) As temperature increases, the MTP (machine learning interatomic potential) framework successfully identifies the evolving phase structures in the combined MC + MD simulation. The phase structure identifiers are determined using the polyhedral template matching modifier in OVITO [78], and orientation details are also included.

with an atomistic lens to interrogate composition-processing-property relationships that have historically required expensive trial-and-error experimentation. The methodology developed here can be extended to other multicomponent alloys where complex phase competition dictates material performance. The key achievements can be summarized as follows:

(1) *Multiscale accuracy.* The MTP achieves mean absolute errors of 1.2 meV/atom for energies and 0.07 eV/Å for forces across Ti-Al-V configurations. Experimental lattice parameters are reproduced within 1%, and elastic constants are predicted within 10% for α-Ti, β-Ti, and Ti_3Al-$D0_{19}$.

(2) *Phase transition predictions.*

(a) The $\alpha \rightarrow \beta$ transition in pure Ti is predicted at 1083 K (6% below the experimental 1155 K).

(b) In Ti-Al systems, $D0_{19}$ stability is observed between 8.5 and 25 at.% Al at 900 to 1200 K, matching CALPHAD predictions.

(c) For Ti-V alloys, $\beta + \omega$ coexistence is identified at 14 to 22 at.% V (200 to 900 K), consistent with experimental observations.

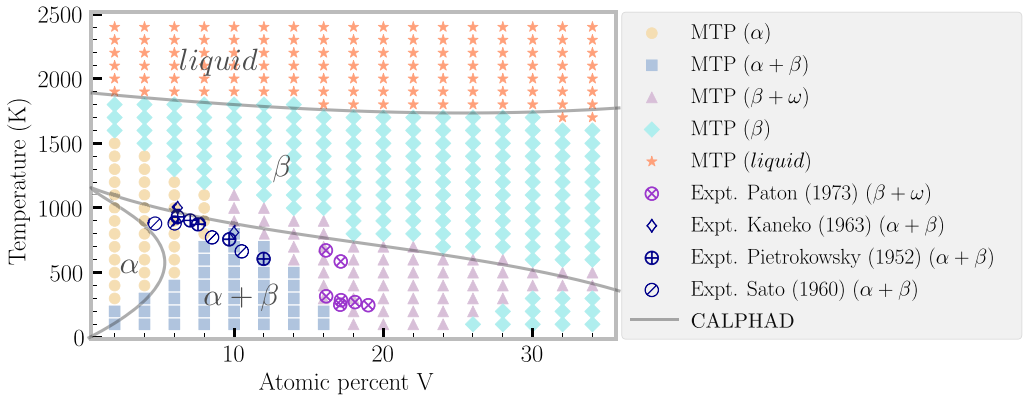

FIG. 12. In a Ti-V system, for varying V concentrations and temperatures, the MTP model predicts phase stability comparable with previous experimental findings. The colored zones correspond to different phases: yellow indicates α, blue indicates $\alpha + \beta$, purple indicates $\beta + \omega$, cyan indicates β, and orange indicates the *liquid* phase. The same colors are used for both MTP predictions and experimental data, distinguished by different marker styles.

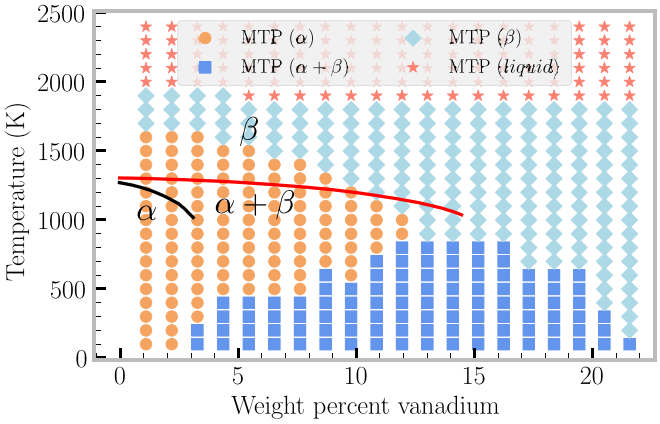

FIG. 13. Phase stability predicted using MTP in Ti6Al-V alloys. Black and red lines are from the schematic of the equilibrium Ti-6Al-4V phase diagram [79].

(3) *Ternary alloy behavior.* Through MD/MC simulations of Ti-6Al-4V:

(a) β-precipitate formation is observed at $>$ 6 at.% V.

(b) Temperature-driven $\beta \rightarrow \alpha \rightarrow \beta$ reversion is captured.

(4) *Computational efficiency.* The optimized MTP achieves a 10$\times$ speedup over RANN potentials and is 3 times slower than MEAM while maintaining DFT accuracy.

(5) *Defect physics in alloys.* The reduction of basal SFE by 32% in Ti-Al systems (112 mJ/m^2 $\rightarrow$ 76 mJ/m^2) is predicted due to Al's promotion of metallic bonding, which allows for better lattice relaxation in the basal slip plane [64], which explains enhanced dislocation pinning.

This work presents the first MLIP developed for the Ti-Al-V ternary system, addressing a critical gap in atomistic modeling capabilities for this commercially vital alloy family. The MTP framework enables previously inaccessible investigations of three key aspects: (1) coupled Al/V solute effects on α/β phase stability, (2) nanoscale precipitate evolution during thermal cycling, and (3) defect-mediated transformation pathways between the α, β, and ω phases. By providing DFT-fidelity predictions at empirical potential speeds, this potential allows researchers to bridge the gap between quantum-scale bonding characteristics (e.g., d-band hybridization in Ti-V) and atomic-scale microstructural evolution—a connection that has remained elusive with traditional modeling approaches. Two transformative applications are now enabled:

(1) Atomistic prediction of β-phase nucleation barriers during quenching processes—critical for heat treatment optimization.

(2) Direct simulation of dislocation-precipitate interactions in Ti-6Al-4V under mechanical loading.

Future work will focus on:

(1) *Database expansion:* Radiation damage cascades and shock compression states will be incorporated to study irradiation effects and high-strain-rate deformation.

(2) *Multiscale validation:* Synergy with phase-field models using MTP-derived interfacial energies and diffusion coefficients, or synergy with discrete dislocation dynamics using MTP-derived dislocation mobility.

DATA AVAILABILITY

The data that support the findings of this article are openly available [80].

[1] I. Gurrappa, Characterization of titanium alloy Ti-6Al-4V for chemical, marine and industrial applications, Mater. Charact. **51**, 131 (2003).

[2] M. Niinomi, Mechanical properties of biomedical titanium alloys, Mater. Sci. Eng.: A **243**, 231 (1998).

[3] S. Semiatin, V. Seetharaman, and I. Weiss, Hot workability of titanium and titanium aluminide alloys–an overview, Mater. Sci. Eng.: A **243**, 1 (1998).

[4] G. Lütjering, Influence of processing on microstructure and mechanical properties of ($\alpha + \beta$) titanium alloys, Mater. Sci. Eng.: A **243**, 32 (1998).

[5] G. Lütjering, J. Williams, and A. Gysler, Microstructure and mechanical properties of titanium alloys, *Microstructure and Properties of Materials* (2000), Vol. 2, pp. 1–77.

[6] R. P. Kolli and A. Devaraj, A review of metastable beta titanium alloys, Metals **8**, 506 (2018).

[7] V. K. Saxena and V. Radhakrishnan, Effect of phase morphology on fatigue crack growth behavior of α-β titanium alloy–a crack closure rationale, Metall. Mater. Trans. A **29**, 245 (1998).

[8] S. Mantri, D. Choudhuri, A. Behera, J. Cotton, N. Kumar, and R. Banerjee, Influence of fine-scale alpha precipitation on the mechanical properties of the beta titanium alloy beta-21S, Metall. Mater. Trans. A **46**, 2803 (2015).

[9] Y. Zheng, R. E. Williams, D. Wang, R. Shi, S. Nag, P. Kami, J. M. Sosa, R. Banerjee, Y. Wang, and H. L. Fraser, Role of ω phase in the formation of extremely refined intragranular α precipitates in metastable β-titanium alloys, Acta Mater. **103**, 850 (2016).

[10] H. Moustahfid, N. Gey, M. Humbert, and M. Philippe, Study of the β-α phase transformations of a Ti-64 sheet induced from a high-temperature β state and a high-temperature $\alpha + \beta$ state, Metall. Mater. Trans. A **28**, 51 (1997).

[11] S. Malinov, P. Markovsky, W. Sha, and Z. Guo, Resistivity study and computer modelling of the isothermal transformation kinetics of Ti–6Al–4V and Ti–6Al–2Sn–4Zr–2Mo–0.08 Si alloys, J. Alloys Compd. **314**, 181 (2001).

[12] D. Wolf, V. Yamakov, S. Phillpot, A. Mukherjee, and H. Gleiter, Deformation of nanocrystalline materials by molecular-dynamics simulation: relationship to experiments? Acta Mater. **53**, 1 (2005).

[13] M. S. Daw, S. M. Foiles, and M. I. Baskes, The embedded-atom method: a review of theory and applications, Mater. Sci. Rep. **9**, 251 (1993).

[14] M. I. Baskes, Modified embedded-atom potentials for cubic materials and impurities, Phys. Rev. B **46**, 2727 (1992).

[15] B.-J. Lee, M. Baskes, H. Kim, and Y. K. Cho, Second nearest-neighbor modified embedded atom method potentials

for bcc transition metals, Phys. Rev. B **64**, 184102 (2001).
[16] J. S. Smith, O. Isayev, and A. E. Roitberg, ANI-1: an extensible neural network potential with DFT accuracy at force field computational cost, Chem. Sci. **8**, 3192 (2017).
[17] J. A. Vita and D. R. Trinkle, Spline-based neural network interatomic potentials: Blending classical and machine learning models, Comput. Mater. Sci. **232**, 112655 (2024).
[18] T. Morawietz and N. Artrith, Machine learning-accelerated quantum mechanics-based atomistic simulations for industrial applications, J. Comput.-Aided Mol. Des. **35**, 557 (2021).
[19] Y. Zuo, C. Chen, X. Li, Z. Deng, Y. Chen, J. Behler, G. Csányi, A. V. Shapeev, A. P. Thompson, M. A. Wood *et al.*, Performance and cost assessment of machine learning interatomic potentials, J. Phys. Chem. A **124**, 731 (2020).
[20] V. L. Deringer, M. A. Caro, and G. Csányi, Machine learning interatomic potentials as emerging tools for materials science, Adv. Mater. **31**, 1902765 (2019).
[21] J. Behler, Perspective: Machine learning potentials for atomistic simulations, J. Chem. Phys. **145**, 170901 (2016).
[22] R. Kobayashi, D. Giofré, T. Junge, M. Ceriotti, and W. A. Curtin, Neural network potential for Al-Mg-Si alloys, Phys. Rev. Mater. **1**, 053604 (2017).
[23] D. Dickel, M. Nitol, and C. Barrett, Lammps implementation of rapid artificial neural network derived interatomic potentials, Comput. Mater. Sci. **196**, 110481 (2021).
[24] M. Nichols, C. D. Barrett, D. E. Dickel, M. S. Nitol, and S. J. Fensin, Predicting Ti-Al binary phase diagram with an artificial neural network potential, arXiv:2411.07960.
[25] A. Chandran, A. Santhosh, C. Pistidda, P. Jerabek, R. C. Aydin, and C. J. Cyron, Comparative analysis of ternary TiAlNb interatomic potentials: moment tensor vs. deep learning approaches, Front. mater. **11**, 1466793 (2024).
[26] I. S. Novikov, Y. V. Suleimanov, and A. V. Shapeev, Automated calculation of thermal rate coefficients using ring polymer molecular dynamics and machine-learning interatomic potentials with active learning, Phys. Chem. Chem. Phys. **20**, 29503 (2018).
[27] F. Tasnadi, F. Bock, J. Tidholm, A. V. Shapeev, and I. A. Abrikosov, Efficient prediction of elastic properties of $Ti_{0.5}Al_{0.5}N$ at elevated temperature using machine learning interatomic potential, Thin Solid Films **737**, 138927 (2021).
[28] K. Gubaev, E. V. Podryabinkin, G. L. Hart, and A. V. Shapeev, Accelerating high-throughput searches for new alloys with active learning of interatomic potentials, Comput. Mater. Sci. **156**, 148 (2019).
[29] J. Qi, Z. Aitken, Q. Pei, A. M. Z. Tan, Y. Zuo, M. Jhon, S. Quek, T. Wen, Z. Wu, and S. P. Ong, Machine learning moment tensor potential for modeling dislocation and fracture in $L1_0$-TiAl and $D0_{19}$-Ti_3Al alloys, Phys. Rev. Mater. **7**, 103602 (2023).
[30] A. V. Shapeev, Moment tensor potentials: A class of systematically improvable interatomic potentials, Multiscale Modeling & Simulation **14**, 1153 (2016).
[31] J. Hafner, *Ab-initio* simulations of materials using VASP: Density-functional theory and beyond, J. Comput. Chem. **29**, 2044 (2008).
[32] J. P. Perdew, K. Burke, and M. Ernzerhof, Generalized gradient approximation made simple, Phys. Rev. Lett. **77**, 3865 (1996).
[33] M. S. Nitol, D. E. Dickel, and C. D. Barrett, Machine learning models for predictive materials science from fundamental physics: An application to titanium and zirconium, Acta Mater. **224**, 117347 (2022).
[34] M. S. Nitol, K. Dang, S. J. Fensin, M. I. Baskes, D. E. Dickel, and C. D. Barrett, Hybrid interatomic potential for Sn, Phys. Rev. Mater. **7**, 043601 (2023).
[35] E. V. Podryabinkin, E. V. Tikhonov, A. V. Shapeev, and A. R. Oganov, Accelerating crystal structure prediction by machine-learning interatomic potentials with active learning, Phys. Rev. B **99**, 064114 (2019).
[36] C. Wang, K. Aoyagi, P. Wisesa, and T. Mueller, Lithium ion conduction in cathode coating materials from on-the-fly machine learning, Chem. Mater. **32**, 3741 (2020).
[37] J. Qi, S. Banerjee, Y. Zuo, C. Chen, Z. Zhu, M. H. Chandrappa, X. Li, and S. P. Ong, Bridging the gap between simulated and experimental ionic conductivities in lithium superionic conductors, Mater. Today Phys. **21**, 100463 (2021).
[38] I. S. Novikov, K. Gubaev, E. V. Podryabinkin, and A. V. Shapeev, The MLIP package: moment tensor potentials with MPI and active learning, Mach. Learn.: Sci. Technol. **2**, 025002 (2020).
[39] A. P. Thompson, H. M. Aktulga, R. Berger, D. S. Bolintineanu, W. M. Brown, P. S. Crozier, P. J. In't Veld, A. Kohlmeyer, S. G. Moore, T. D. Nguyen *et al.*, LAMMPS-a flexible simulation tool for particle-based materials modeling at the atomic, meso, and continuum scales, Comput. Phys. Commun. **271**, 108171 (2022).
[40] A. Stukowski, Visualization and analysis of atomistic simulation data with OVITO–the open visualization tool, Modell. Simul. Mater. Sci. Eng. **18**, 015012 (2009).
[41] N. W. Ashcroft, N. D. Mermin, and S. Rodriguez, Solid state physics, Am. J. Phys. **46**, 116 (1978).
[42] C. Kittel, *Introduction to Solid State Physics* (John Wiley & Sons, Hoboken, 2005), p. 680.
[43] W. B. Pearson, *A Handbook of Lattice Spacings and Structures of Metals and Alloys: International Series of Monographs on Metal Physics and Physical Metallurgy* (Elsevier, 2013), Vol. 4.
[44] Y. He, R. Schwarz, T. Darling, M. Hundley, S. Whang, and Z. Wang, Elastic constants and thermal expansion of single crystal γ-tial from 300 to 750 k, Mater. Sci. Eng.: A **239-240**, 157 (1997).
[45] R. R. Zope and Y. Mishin, Interatomic potentials for atomistic simulations of the Ti-Al system, Phys. Rev. B **68**, 024102 (2003).
[46] D. Farkas, Interatomic potentials for Ti-Al with and without angular forces, Modell. Simul. Mater. Sci. Eng. **2**, 975 (1994).
[47] Y.-K. Kim, H.-K. Kim, W.-S. Jung, and B.-J. Lee, Atomistic modeling of the Ti–Al binary system, Comput. Mater. Sci. **119**, 1 (2016).
[48] Q.-X. Pei, M. Jhon, S. S. Quek, and Z. Wu, A systematic study of interatomic potentials for mechanical behaviours of Ti-Al alloys, Comput. Mater. Sci. **188**, 110239 (2021).
[49] D. Marchand and W. Curtin, Machine learning for metallurgy IV: A neural network potential for Al-Cu-Mg and Al-Cu-Mg-Zn, Phys. Rev. Mater. **6**, 053803 (2022).
[50] G. Simmons, Single crystal elastic constants and calculated aggregate properties, J. Grad. Res. Ctr. **34**, 1 (1965).
[51] G. Simmons and H. Wang, *Single Crystal Elastic Constants and Calculated Aggregate Properties: A Handbook* (MIT Press, 1971).

[52] K. Tanaka, K. Okamoto, H. Inui, Y. Minonishi, M. Yamaguchi, and M. Koiwa, Elastic constants and their temperature dependence for the intermetallic compound Ti_3Al, Philosophical Magazine A **73**, 1475 (1996).

[53] E. Fisher and C. Renken, Single-crystal elastic moduli and the hcp→ bcc transformation in Ti, Zr, and Hf, Phys. Rev. **135**, A482 (1964).

[54] A. Togo, F. Oba, and I. Tanaka, First-principles calculations of the ferroelastic transition between rutile-type and $CaCl_2$-type SiO_2 at high pressures, Phys. Rev. B **78**, 134106 (2008).

[55] W. Petry, A. Heiming, J. Trampenau, M. Alba, C. Herzig, H. Schober, and G. Vogl, Phonon dispersion of the bcc phase of group-iv metals. I. bcc titanium, Phys. Rev. B **43**, 10933 (1991).

[56] M. S. Nitol, M. J. Echeverria, K. Dang, M. I. Baskes, and S. J. Fensin, New modified embedded-atom method interatomic potential to understand deformation behavior in vnbtatizr refractory high entropy alloy, Comput. Mater. Sci. **237**, 112886 (2024).

[57] L. Mezey and J. Giber, The surface free energies of solid chemical elements: Calculation from internal free enthalpies of atomization, Jpn. J. Appl. Phys. **21**, 1569 (1982).

[58] H. E. Schaefer, R. Gugelmeier, M. Schmolz, and A. Seeger, Positron lifetime spectroscopy and trapping at vacancies in aluminium, Materials Science Forum **15**, 111 (1987).

[59] F. R. de Boer, W, C. M. Mattens, R. Boom, A. R. Miedema, and A. K. Niessen, *Cohesion in Metals* (North Holland, 2025), Vol. 1.

[60] W. R. Tyson and W. A. Miller, Surface free energies of solid metals: Estimation from liquid surface tension measurements, Surf. Sci. **62**, 267 (1977).

[61] W. F. Gale and T. C. Totemeier, *Smithells Metals Reference Book (8th Edition)* (Elsevier, 2004).

[62] See Supplemental Material at http://link.aps.org/supplemental/10.1103/PhysRevMaterials.9.063601 for decohesion energy curves for unary and binary subsystems are presented to illustrate interfacial energetics among Ti, Al, and V configurations. Also, the computational efficiency of MTP is assessed by conducting molecular dynamics simulations of Ti + 6% Al systems using MEAM, MTP, and RANN interatomic potentials.

[63] M. S. Nitol, D. E. Dickel, and S. J. Fensin, Neural network interatomic potential-driven analysis of phase stability in Ti–V alloys at the atomistic scale, Mater. Today Commun. **41**, 110332 (2024).

[64] P. Kwasniak, H. Garbacz, and K. Kurzydlowski, Solid solution strengthening of hexagonal titanium alloys: Restoring forces and stacking faults calculated from first principles, Acta Mater. **102**, 304 (2016).

[65] D. A. Young, *Phase Diagrams of the Elements* (University of California Press, Berkeley, 2023).

[66] J. Zhang, Y. Zhao, R. S. Hixson, G. T. Gray III, L. Wang, W. Utsumi, S. Hiroyuki, and H. Takanori, Experimental constraints on the phase diagram of titanium metal, J. Phys. Chem. Solids **69**, 2559 (2008).

[67] W.-S. Ko, B. Grabowski, and J. Neugebauer, Development and application of a Ni-Ti interatomic potential with high predictive accuracy of the martensitic phase transition, Phys. Rev. B **92**, 134107 (2015).

[68] T. Lee, M. I. Baskes, S. M. Valone, and J. Doll, Atomistic modeling of thermodynamic equilibrium and polymorphism of iron, J. Phys.: Condens. Matter **24**, 225404 (2012).

[69] S. Sikka, Y. Vohra, and R. Chidambaram, Omega phase in materials, Prog. Mater. Sci. **27**, 245 (1982).

[70] B. Sadigh, P. Erhart, A. Stukowski, A. Caro, E. Martinez, and L. Zepeda-Ruiz, Scalable parallel Monte Carlo algorithm for atomistic simulations of precipitation in alloys, Phys. Rev. B **85**, 184203 (2012).

[71] N. Metropolis, A. W. Rosenbluth, M. N. Rosenbluth, A. H. Teller, and E. Teller, Equation of state calculations by fast computing machines, J. Chem. Phys. **21**, 1087 (1953).

[72] V. Witusiewicz, A. Bondar, U. Hecht, S. Rex, and T. Y. Velikanova, The Al–B–Nb–Ti system: III. Thermodynamic re-evaluation of the constituent binary system Al–Ti, J. Alloys Compd. **465**, 64 (2008).

[73] R. Chinnappan, B. Panigrahi, and A. van de Walle, First-principles study of phase equilibrium in Ti–V, Ti–Nb, and Ti–Ta alloys, Calphad **54**, 125 (2016).

[74] H. Kaneko and Y. C. Huang, Allotropic transformation characteristics of titanium alloys during continuous cooling, *Nippon Kinzoku Gakkaishi* (Japan,1963), Vol. 27.

[75] P. Pietrokowsky and P. Duwez, Partial titanium-vanadium phase diagram, JOM **4**, 627 (1952).

[76] T. Sato, S. Hukai, and Y. C. Huang, The ms points of binary titanium alloys, J. Aust. Inst. Met. **5**, 149 (1960).

[77] N. Paton and J. Williams, The influence of oxygen content on the athermal β-ω transformation, Scr. Metall. **7**, 647 (1973).

[78] P. M. Larsen, S. Schmidt, and J. Schiøtz, Robust structural identification via polyhedral template matching, Modell. Simul. Mater. Sci. Eng. **24**, 055007 (2016).

[79] T. Majumdar, T. Bazin, E. Massahud Carvalho Ribeiro, J. E. Frith, and N. Birbilis, Understanding the effects of pbf process parameter interplay on Ti-6Al-4V surface properties, PLoS One **14**, e0221198 (2019).

[80] https://gitlab.com/mtp_potentials/tialv.